

Lensless wide-field fluorescent imaging on a chip using compressive decoding of sparse objects

Ahmet F. Coskun^{1,3}, Ikbal Sencan^{1,3}, Ting-Wei Su^{1,3}, and Aydogan Ozcan^{1,2,*}

¹Electrical Engineering Department, University of California, Los Angeles, CA, USA

²California NanoSystems Institute, University of California, Los Angeles, CA, USA

³These authors contributed equally to this work.

*ozcan@ucla.edu

<http://innovate.ee.ucla.edu/>

Abstract: We demonstrate the use of a compressive sampling algorithm for on-chip fluorescent imaging of sparse objects over an ultra-large field-of-view ($>8 \text{ cm}^2$) without the need for any lenses or mechanical scanning. In this lensfree imaging technique, fluorescent samples placed on a chip are excited through a prism interface, where the pump light is filtered out by total internal reflection after exciting the entire sample volume. The emitted fluorescent light from the specimen is collected through an on-chip fiber-optic faceplate and is delivered to a wide field-of-view opto-electronic sensor array for lensless recording of fluorescent spots corresponding to the samples. A compressive sampling based optimization algorithm is then used to rapidly reconstruct the sparse distribution of fluorescent sources to achieve $\sim 10 \text{ }\mu\text{m}$ spatial resolution over the entire active region of the sensor-array, i.e., over an imaging field-of-view of $>8 \text{ cm}^2$. Such a wide-field lensless fluorescent imaging platform could especially be significant for high-throughput imaging cytometry, rare cell analysis, as well as for micro-array research.

©2010 Optical Society of America

OCIS codes: (110.2970) Image detection systems; (170.2520) Fluorescence Microscopy.

References and links

1. E. J. Candès, J. K. Romberg, and T. Tao, "Stable signal recovery from incomplete and inaccurate measurements," *Commun. Pure Appl. Math.* **59**(8), 1207–1223 (2006).
2. E. J. Candès, and T. Tao, "Near-optimal signal recovery from random projections: Universal encoding strategies?" *IEEE Trans. Inf. Theory* **52**(12), 5406–5425 (2006).
3. D. L. Donoho, "Compressed sensing," *IEEE Trans. Inf. Theory* **52**(4), 1289–1306 (2006).
4. D. J. Brady, *Optical Imaging and Spectroscopy*, (Wiley, 2009).
5. J. Stinnett, and J. Gillenwater, "NIR Single Pixel Camera," *Connexions*, <http://cnx.org/content/col110525/1.1/>, (2008).
6. D. Takhar, J. N. Laska, M. B. Wakin, M. F. Duarte, D. Baron, S. Sarvotham, K. F. Kelly, and R. G. Baraniuk, "A new compressive imaging camera architecture using optical-domain compression," in *Computational Imaging IV*, 6065, (San Jose, CA, USA), p. 606509, SPIE, (2006).
7. M. F. Duarte, M. A. Davenport, D. Takhar, J. N. Laska, Ting Sun, K. F. Kelly, and R. G. Baraniuk, "Single-pixel imaging via compressive sampling," *IEEE Signal Process. Mag.* **25**(2), 83–91 (2008).
8. M. E. Gehm, R. John, D. J. Brady, R. M. Willett, and T. J. Schulz, "Single-shot compressive spectral imaging with a dual-disperser architecture," *Opt. Express* **15**(21), 14013–14027 (2007).
9. A. Wagadarikar, R. John, R. Willett, and D. J. Brady, "Single disperser design for coded aperture snapshot spectral imaging," *Appl. Opt.* **47**(10), B44–B51 (2008).
10. W. L. Chan, M. L. Moravec, R. G. Baraniuk, and D. M. Mittleman, "Terahertz imaging with compressed sensing and phase retrieval," *Opt. Lett.* **33**(9), 974–976 (2008).
11. J. Romberg, "Imaging via Compressive Sampling," *IEEE Signal Process. Mag.* **25**(2), 14–20 (2008).
12. M. Sheikh, O. Milenkovic, and R. Baraniuk, "Designing compressive sensing DNA microarrays" *IEEE Workshop on Computational Advances in Multi-Sensor Adaptive Processing (CAMSAP)*, St. Thomas, U.S. Virgin Islands, December (2007)
13. M. Lustig, D. Donoho, and J. M. Pauly, "Sparse MRI: The application of compressed sensing for rapid MR imaging," *Magn. Reson. Med.* **58**(6), 1182–1195 (2007).
14. D. J. Brady, K. Choi, D. L. Marks, R. Horisaki, and S. Lim, "Compressive holography," *Opt. Express* **17**(15), 13040–13049 (2009).

15. L. Denis, D. Lorenz, E. Thiébaud, C. Fournier, and D. Trede, "Inline hologram reconstruction with sparsity constraints," *Opt. Lett.* **34**(22), 3475–3477 (2009).
16. H. Yu, and G. Wang, "Compressed sensing based interior tomography," *Phys. Med. Biol.* **54**(9), 2791–2805 (2009).
17. Y. Lu, X. Zhang, A. Douraghy, D. Stout, J. Tian, T. F. Chan, and A. F. Chatzioannou, "Source reconstruction for spectrally-resolved bioluminescence tomography with sparse a priori information," *Opt. Express* **17**(10), 8062–8080 (2009).
18. H. Gao, and H. Zhao, "Multilevel bioluminescence tomography based on radiative transfer equation Part 1: 11 regularization," *Opt. Express* **18**(3), 1854–1871 (2010).
19. A. F. Coskun, T. W. Su, and A. Ozcan, "Wide field-of-view lens-free fluorescent imaging on a chip," *Lab Chip* **10**(7), 824–827 (2010).
20. S. Nagrath, L. V. Sequist, S. Maheswaran, D. W. Bell, D. Irimia, L. Ulkus, M. R. Smith, E. L. Kwak, S. Digumarthy, A. Muzikansky, P. Ryan, U. J. Balis, R. G. Tompkins, D. A. Haber, and M. Toner, "Isolation of rare circulating tumour cells in cancer patients by microchip technology," *Nature* **450**(7173), 1235–1239 (2007).
21. S. K. Murthy, A. Sin, R. G. Tompkins, and M. Toner, "Effect of flow and surface conditions on human lymphocyte isolation using microfluidic chambers," *Langmuir* **20**(26), 11649–11655 (2004).
22. A. A. Adams, P. I. Okagbare, J. Feng, M. L. Hupert, D. Patterson, J. Göttert, R. L. McCarley, D. Nikitopoulos, M. C. Murphy, and S. A. Soper, "Highly efficient circulating tumor cell isolation from whole blood and label-free enumeration using polymer-based microfluidics with an integrated conductivity sensor," *J. Am. Chem. Soc.* **130**(27), 8633–8641 (2008).
23. S. J. Tan, L. Yobas, G. Y. H. Lee, C. N. Ong, and C. T. Lim, "Microdevice for the isolation and enumeration of cancer cells from blood," *Biomed. Microdevices* **11**(4), 883 (2009).
24. E. Betzig, G. H. Patterson, R. Sougrat, O. W. Lindwasser, S. Olenych, J. S. Bonifacino, M. W. Davidson, J. Lippincott-Schwartz, and H. F. Hess, "Imaging intracellular fluorescent proteins at nanometer resolution," *Science* **313**(5793), 1642–1645 (2006).
25. M. J. Rust, M. Bates, and X. Zhuang, "Sub-diffraction-limit imaging by stochastic optical reconstruction microscopy (STORM)," *Nat. Methods* **3**(10), 793–796 (2006).
26. S.-J. Kim, K. Koh, M. Lustig, S. Boyd, and D. Gorinevsky, "An Interior-Point Method for Large-Scale 11-Regularized Least Squares," *IEEE J. Sel. Top. Signal Processing* **1**(4), 606–617 (2007).
27. S. Seo, T. W. Su, D. K. Tseng, A. Erlinger, and A. Ozcan, "Lensfree holographic imaging for on-chip cytometry and diagnostics," *Lab Chip* **9**(6), 777–787 (2009).
28. C. Oh, S. O. Isikman, B. Khademhosseini, and A. Ozcan, "On-chip differential interference contrast microscopy using lensless digital holography," *Opt. Express* **18**(5 Issue 5), 4717–4726 (2010).
29. W. H. Richardson, "Bayesian-Based Iterative Method of Image Restoration," *J. Opt. Soc. Am.* **62**(1), 55–59 (1972).
30. L. B. Lucy, "An iterative technique for the rectification of observed distributions," *Astron. J.* **79**, 745–754 (1974).
31. D. S. C. Biggs, and M. Andrews, "Acceleration of iterative image restoration algorithms," *Appl. Opt.* **36**(8), 1766–1775 (1997).

1. Introduction

Compressive sampling (also known as compressive sensing) [1–3] is a recently emerging field that in general aims to recover a function (i.e., a signal) from many fewer measurements/samples than normally required according to the Shannon's sampling theorem. This emerging theory has been recently applied to various fields to bring new insights to measurement and imaging science [4–18]. As an example, it has been used to create a single pixel camera that is especially valuable for imaging at different parts of the electro-magnetic spectrum where high-density-pixel imagers are not readily available or are highly costly [5–7]. Among many others, another recent achievement of this theory in photonics was the use of compressive decoding in holographic reconstruction of a 3D object volume [14,15].

In this manuscript, we introduce a new on-chip fluorescent imaging modality that utilizes a compressive sampling based algorithm to achieve $\sim 10\mu\text{m}$ spatial resolution for imaging of sparse objects over an ultra-large field of view of $>8\text{cm}^2$ without the use of any lenses or mechanical scanning. In this approach (see Fig. 1), fluorescent samples, positioned e.g., within a micro-channel, are pumped through a prism interface, where the excitation light (in the form of propagating waves) faces total internal reflection after exciting the entire sample volume. The fluorescent emission from the excited micro-objects is then collected using a dense fiber-optic faceplate and is delivered to a large format opto-electronic sensor array without the use of any lenses. This detected lensfree fluorescent image does not have any physical magnification and therefore has a field-of-view (FOV) that is equivalent to the detector active area, covering $>8\text{cm}^2$ (see Fig. 1). On the other hand, because of its lensless operation, the detected fluorescent spots are significantly enlarged and distorted due to free

space propagation, large pixel size, as well as the faceplate operation. We demonstrate that these distortions can be significantly eliminated by using a digital reconstruction/decoding algorithm that is based on compressive sampling theory to achieve $\sim 10\mu\text{m}$ spatial resolution across the entire detector active area. When compared to our earlier lensfree fluorescent imaging report [19], our new results present an improvement of ~ 5 fold in spatial resolution without a trade-off in FOV, which we attribute to the use of the fiber-optic faceplate and the compressive sampling based numerical processing. Furthermore, with this new on-chip platform, we also demonstrate lensfree fluorescent imaging of *vertically stacked* micro-channels, all in parallel, further increasing the throughput of fluorescent on-chip imaging.

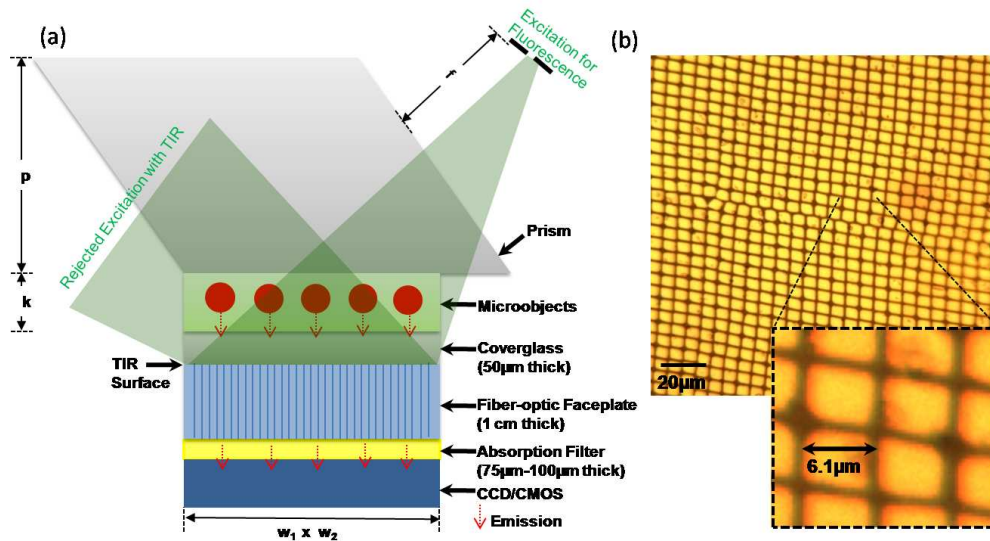


Fig. 1. (a) Schematic diagram of the lensfree on-chip fluorescent imaging platform is shown. Drawing is not to scale. This imaging platform has unit magnification such that the imaging field-of-view equals to the entire active area of the sensor array (i.e., $>8\text{ cm}^2$). The TIR condition occurs at the glass-air interface at the bottom facet of the coverglass. To avoid detection of scattered pump photons a plastic absorption filter is used after the faceplate. Typical dimensions: $w_1 \times w_2 = 25\text{mm} \times 35\text{mm}$; $p = 1.7\text{ cm}$; $k \sim 10\text{-}100\ \mu\text{m}$; $f = 1\text{-}2\text{ cm}$. (b) A microscope image of the faceplate is shown. The numerical aperture of each fiber is ~ 0.3 .

This on-chip fluorescent imaging platform, being lensfree and compact, together with a powerful compressive sampling algorithm behind it, would especially be valuable for high-throughput imaging of cells within micro-fluidic chips. Specifically, it would be quite important for *cytometry* applications involving e.g., rare-cell analysis in large area micro-fluidic devices. In such rare-cell analysis applications [20–23], the target cells of interest (e.g., circulating tumor cells in whole blood samples) occur at extremely low concentrations which make their corresponding images *highly sparse*, providing an important connection to compressive sampling. Therefore, the presented fluorescent on-chip imaging technique, having an ultra-wide FOV of $>8\text{ cm}^2$ within a lensfree compact platform, would be quite valuable to rapidly screen large area micro-fluidic devices to quantify the capture of specific cells at extreme rare statistics, providing a useful tool for high-throughput cytometry. Furthermore, as we demonstrate in this work, our platform also permits simultaneous imaging of vertically stacked micro-channels on the same chip, which is another step forward towards increasing the fluorescent imaging throughput. Our approach could also potentially impact micro-array imaging technologies by providing lensless quantification of hundreds of thousands of micro-spots, all in parallel, within a compact chip.

Finally, we would like to also point out the possibility that the compressive fluorescence decoding approach used in this work may also be extended to *lens-based* fluorescent microscopy, and in particular to recent fluorescent super-resolution approaches including

PALM and STORM [24,25] to potentially reduce the number of frames that is required for 2D or 3D fluorescent imaging. Such a compressive decoding approach, however, would need to be carefully tested in terms of achievable localization accuracy and potential artifacts for multiple fluorescent points located within a diffraction limited spot.

2. Lensfree fluorescent imaging on a chip and compressive sampling relationship

To briefly go over the relationship between lensfree fluorescent imaging on a chip and compressive sampling theory, let us denote the fluorescent particle/cell distribution within the sample volume with $\bar{c} = [c_1, c_2, \dots, c_N]$ where N denotes the number of voxels. To better relate our model to a real imaging experiment, let us also assume that the physical grid size in \bar{c} is d . For visualization purposes, one can think of a simple microfluidic channel such that \bar{c} would represent the points on the active surface of the channel, where the captured cells reside within an imaging area of $N \times d^2$. For multi-layered micro-channels, however, \bar{c} would represent a 3D discrete volume.

For the applications that are of interest to this work, such as wide-field fluorescent cytometry, rare cell analysis and high-throughput micro-array imaging, one can in general assume that \bar{c} is *sparse* to start with, such that only S coefficients of \bar{c} are non-zero, where $S \ll N$. This assumption is further justified with our unit magnification lensless geometry since most cells of interest would not be over-sampled due to limited spatial resolution, restricting the value of S for a practical \bar{c} . Therefore, the sparsity of \bar{c} is the first connection to compressive sampling, as it is an important requirement of its underlying theory [1–3].

In a lensfree fluorescent imaging platform as shown in Fig. 1(a), \bar{c} uniquely determines the intensity distribution that is impinging on the detector-array. For each non-zero element of \bar{c} , a wave is transmitted, and after passing through different layers on the chip it incoherently adds up with the waves created by the other fluorescent points within the sample volume. Therefore, one can write the intensity distribution right above the detector plane (*before* being measured/sampled) as:

$$f(x, y) = \sum_{i=1}^N c_i \psi_i(x, y) \quad (1)$$

where $\psi_i(x, y)$ represents the 2D wave intensity right before the detector plane that originated from the physical location of c_i . The analytical form of ψ_i can be derived for any particular lensfree geometry such as the one presented in Fig. 1(a). However, from a practical point of view, it can easily be measured for each object plane by using e.g., small fluorescent particles, which is the approach taken in this work.

Without the use of a faceplate in Fig. 1(a), it is straightforward to see that the functional form of ψ_i for a given object plane is space invariant. This is equivalent to say that $\psi_i(x, y) = p(x - x_i, y - y_i)$, where $p(x, y)$ is the incoherent point-spread function (psf) of the system for a given object layer, and (x_i, y_i) denotes the physical location of c_i . Note that in this definition, $p(x, y)$ has no relationship to the pixel size at the detector since Eq. (1) describes the intensity right before the sampling plane. The same space invariance property also holds with a *dense* fiber-optic faceplate as shown in Fig. 1(a) since there is a significant gap between the sample and faceplate planes, and a similar gap between the bottom surface of the faceplate and the detector plane. Therefore for our lensfree fluorescent imaging geometry of Fig. 1(a), with or without the faceplate operation, one can in general write:

$$f(x, y) = \sum_{i=1}^N c_i p(x - x_i, y - y_i) \quad (2)$$

For multiple layers of fluorescent objects, a similar equation could also be written where the incoherent point-spread function of different layers are also included in the summation.

Equation (2) relates the “already” sparse fluorescent object distribution (\bar{c}) to an optical intensity distribution that is yet to be sampled by the detector array. The representation basis provided by $\psi_i(x, y)$ is surely not an orthogonal one since it is based on lensfree diffraction. This is not limiting the applicability of compressive decoding to our work since \bar{c} is assumed to be already sparse, independent of the representation basis. On the other hand, the fact that $\psi_i(x, y)$ does not form an orthogonal basis limits the spatial resolution that can be compressively decoded, since for closely spaced c_i values, the corresponding $\psi_i(x, y)$ would be quite similar to each other for a given detection signal to noise ratio (SNR). This is related to the restricted isometry property [1,2] of our system as will be discussed later on; however its physical implication is nothing new since it is already known that we trade off spatial resolution to achieve wide-field lensfree fluorescent imaging with unit magnification.

Next, sampling of $f(x, y)$ at the detector-array can be formulated as:

$$I_m = \iint f(x, y) \cdot \phi(x - x_m, y - y_m) \cdot dx \cdot dy \quad (3)$$

where $\Phi_m = \phi(x - x_m, y - y_m)$ represents the sampling/measurement basis; $m=1:M$ denotes the m^{th} pixel of the detector-array with center coordinates of (x_m, y_m) ; and $\phi(x, y)$ represents the pixel function, which can be approximated to be a detection constant, K , for $|x|, |y| \leq W/2$ (assuming a square pixel size of W) and 0 elsewhere, $|x|, |y| > W/2$. In this notation, the fill-factor of the detector-array together with the quantum efficiency etc are all lumped into K . Note that in this work, we have used $W=9 \mu\text{m}$ and $W=18 \mu\text{m}$ (through pixel binning).

With these definitions, the lensfree fluorescent imaging problem of this manuscript can be summarized as such: based on M independent measurements of I_m , we would like to estimate the sparse fluorescent source distribution, \bar{c} , at the sample.

To give more insight, Eq. (3) models a hypothetical near-field sampling experiment, where each pixel of the CCD measures part of $f(x, y)$. For an *arbitrary* intensity distribution $f(x, y)$ impinging on the detector array, a few pixel values (I_m) can surely *not* represent the entire function. However, if the sampled intensity profile at the detector plane is created by a *sparse* distribution of incoherent point sources located in the far-field, then much fewer pixels can *potentially* be used to recover the source distribution based on compressive decoding. For this decoding to work efficiently, each pixel should ideally detect “some” contribution from all the c_i values, which implies the need for a relatively wide point spread function. However since spreading of the fluorescence also decreases the signal strength at the detector plane, the optimum extent of the point spread function is practically determined by the detection SNR. On one extreme, if the same *sparse* source distribution (\bar{c}) was hypothetically placed in direct contact with the CCD pixels, this would *not* permit any compressive decoding since each incoherent point source can now only contribute to a *single* pixel value. For instance two sub-pixel point sources that are located on the same pixel would only contribute to that particular pixel, which would make their separation physically *impossible* regardless of the measurement SNR. However, the same two sub-pixel point sources could be separated from each other through compressive decoding if they were placed some distance above the detector plane, such that more pixels could detect weighted contributions of their emission.

Since we are considering non-adaptive imaging here (i.e., no *a priori* information about the possible x-y locations of the fluorescent particles/cells), we have not used a sub-set of the pixel values (I_m) to reconstruct \bar{c} . Therefore, for a single layer of object, using a unit magnification as in Fig. 1, we have $N \times d^2 = M \times W^2$. In this work, to claim a spatial resolution of $\sim 10 \mu\text{m}$ at the object plane, we used $d = 2-3 \mu\text{m}$, which implies $N \geq 9M$ for $W=9 \mu\text{m}$. For some experiments, we have also used a pixel size of $W=18 \mu\text{m}$ with $d=2 \mu\text{m}$, implying $N=81M$. Furthermore, for multi-layer experiments (to be reported in the next section) where 3 different fluorescent channels were vertically stacked and simultaneously imaged in a single

snap-shot, we had $N=27M$, which all indicate *compressive imaging* since the number of measurements (M) are significantly smaller than the number of reconstructed points (N).

As already known in compressive sampling literature, the effectiveness of the decoding process to estimate \bar{c} in our technique should also depend on the maximum spatial correlation between Φ_m and ψ_i for all possible $m=1:M$ and $i=1:N$ pairs. Accordingly, this maximum spatial correlation coefficient defines the measure of incoherence between sampling and representation bases, which can then be related to the probability of accurately reconstructing \bar{c} from M measurements [1–3]. For a given object plane, because of the shift invariant nature of both Φ_m and ψ_i , this coherence calculation is equivalent to calculation of the correlation between the pixel function $\phi(x,y)$ and the incoherent point-spread function $p(x,y)$. The smaller the correlation between these two spatial functions is, the more accurate and efficient the compressive decoding process gets. Based on this, a smaller pixel size would further help in our lensfree on-chip scheme by reducing this maximum correlation coefficient, i.e., increasing incoherence between Φ_m and ψ_i .

Thus, we can conclude that the primary function of compressive sampling in this work is to *digitally* undo the effect of diffraction induced spreading formulated in Eqs. (1)–(2) through decoding of lensfree image pixels indicated in Eq. (3). Such a decoding process, however, can also be done *physically* rather than digitally, through the use of a lens (as in conventional fluorescent microscopy at the cost of reduced FOV) or through the use of a faceplate as we demonstrate in this work. The use of the faceplate in Fig. 1 *partially* decodes the diffraction induced spreading, which also relatively increases the correlation between $\phi(x,y)$ and $p(x,y)$, since $p(x,y)$ gets narrower and stronger with the faceplate. Despite this relatively increased coherence between the sampling and representation bases, the improvement in the detection SNR with the faceplate enables better measurement of $p(x,y)$ as well as I_m values, which then improves the accuracy of the compressive decoding process in terms of achievable spatial resolution. This will be further quantified in experimental results presented in the next section.

Finally, we would like mention that the above analysis could be also done using a different set of measurement and representation bases without changing the end conclusions. In the above analysis, we did *not* include the diffraction process as part of the measurement, and therefore the measurement basis only involved the pixel sampling at the detector-array. As an alternative notation, we could have also used $\psi_i(x,y) = \delta(x-x_i, y-y_i)$ for the representation basis, which implies that Ψ is an identity matrix. This is not a surprising choice since the object, \bar{c} is already sparse and therefore the sparsifying matrix can be seen as an identity matrix. Based on this definition of the representation basis, the measurement basis Φ_m will now need to include both the diffraction and the pixel sampling processes. Following a similar derivation as in Eq. (3), the measurement basis now becomes: $\Phi_m = \iint p(x-x_i, y-y_i) \cdot \phi(x-x_m, y-y_m) \cdot dx \cdot dy$. As expected, the correlation behavior between Φ_m and ψ_i for all possible m and i pairs remains the same as before, yielding the same set of conclusions that we arrived using the previously discussed choice of bases.

While it is just a matter of notation, with this new pair of bases, it is also easier to qualitatively relate the spatial resolution to restricted isometry property (RIP) of the system. RIP is a measure of the robustness of sparse signal reconstruction for $N>M$ and $S \ll N$ [1–3]. For this new choice of bases, RIP holds if all the possible subsets of S *columns* taken from $\Phi\Psi = \Phi$ are nearly orthogonal to each other. Assuming that the pixel size is much narrower than the incoherent psf of the object layer of interest, we can then approximate:

$$\Phi_m \approx p(x_m - x_i, y_m - y_i) \cdot \iint \phi(x - x_m, y - y_m) \cdot dx \cdot dy = K \cdot W^2 \cdot p(x_m - x_i, y_m - y_i)$$

Therefore for RIP to hold in this lensfree system, for any arbitrary S choices of $i = 1:N$, the sub-set of functions $\Phi_m \approx K \cdot W^2 \cdot p(x_m - x_i, y_m - y_i)$ should be nearly orthogonal in

(x_m, y_m) . If one purely relies on diffraction, this condition can be harder to satisfy for densely spaced (x_i, y_i) which practically limits the achievable spatial resolution for a given detection SNR. Once again, physically this is not surprising since it is already known that we trade off resolution to achieve wide-field lensfree fluorescent imaging on a chip. Structured surfaces could potentially help achieving a better resolution by randomly breaking the space invariance of the incoherent psf, which is not going to be covered within the context of this manuscript.

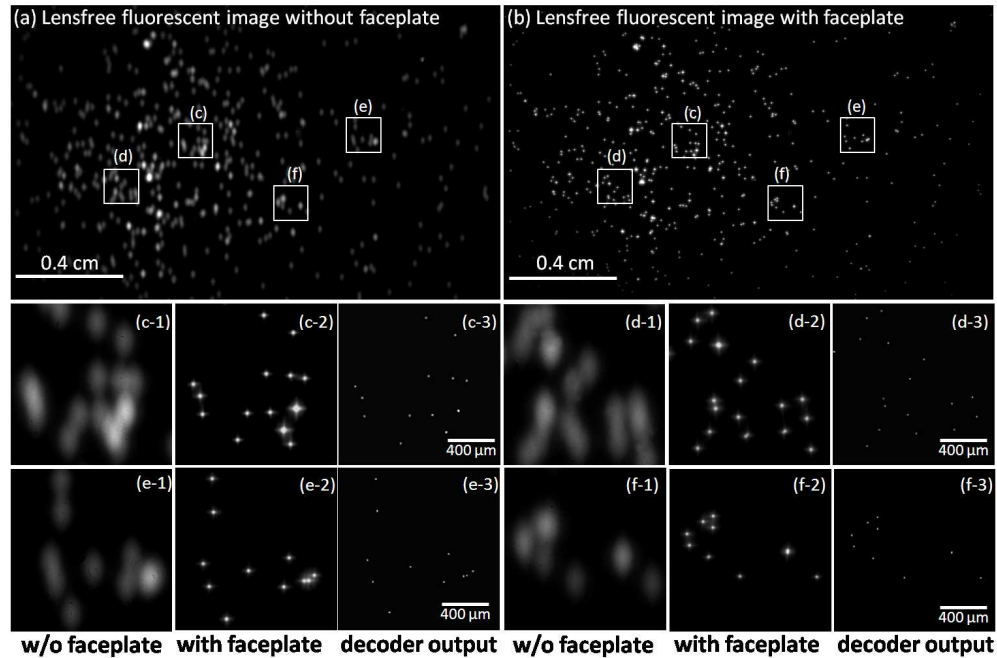


Fig. 2. (a-b) Lensfree fluorescent images of $10\ \mu\text{m}$ particles are compared with and without the faceplate. To make this comparison fair, except the faceplate, all the other dimensions in Fig. 1(a) are kept the same in both of these experiments. With the use of the faceplate, the spatial spreading of the fluorescent signatures at the CCD plane is reduced from $\sim 180\ \mu\text{m}$ down to $\sim 36\ \mu\text{m}$ (FWHM). This improvement is also evident in the comparison that is provided by the digitally zoomed regions shown in (c1-f1) and (c2-f2), which correspond to experiments “without the faceplate” and “with the faceplate”, respectively. The same zoomed images of (c2-f2) are also decoded using a compressive sampling algorithm to yield (c3-f3). As further quantified in Figs. 4, 5 and 6 this compressive decoding process improves the spatial resolution down to $\sim 10\ \mu\text{m}$ all across the field of view of the sensor.

3. Experimental results and discussion

To validate and quantify the performance of our on-chip imaging technique, we imaged fluorescent micro-particles ($2\ \mu\text{m}$ and $10\ \mu\text{m}$ diameter, Excitation: $495\ \text{nm}$, Emission: $505\ \text{nm}$) using the lensfree set-up of Fig. 1(a). In this set-up, we used a large format CCD (KAI-11002 from Kodak, pixel size: $9\ \mu\text{m}$, active area: $25\ \text{mm} \times 35\ \text{mm}$) together with a fiber-optic faceplate where the numerical aperture of each fiber was ~ 0.3 with a period of $\sim 6\ \mu\text{m}$ [see Fig. 1(b)]. The results of these on-chip fluorescent imaging experiments are summarized in Figs. 2–8, which point to several important features of our platform.

First, the comparison provided in Figs. 2(a) and 2(b) indicates that the fiber-optic faceplate in our imaging geometry (Fig. 1) significantly reduces the diffraction induced spreading of the fluorescent signatures of the objects. Specifically, based on Fig. 2 we conclude that the FWHM of the fluorescent signatures at the detector plane is now reduced by ~ 5 fold, from $\sim 180\ \mu\text{m}$ down to $\sim 36\ \mu\text{m}$ using the faceplate (note that except the faceplate thickness, all the other vertical distances are kept the same in both configurations - with and without the

faceplate - to provide a fair comparison). This improvement is quite important as it permits a better detection SNR and a higher spatial resolution to be achieved, which will be further quantified in the next figures.

The physical function of the faceplate used in our experiments is to collect the fluorescent emission from the specimen with an effective numerical aperture of ~ 0.3 and to guide it to the detector array. However, since the fluorescent emission from the objects spreads with an effective numerical aperture of 1 over the air gap above the faceplate, several oblique fluorescent rays (corresponding to higher angles than the acceptance NA of each fiber) remain unguided. These unguided rays (which undergo various partial reflections over multiple fiber cross-sections) are also detected at the sensor plane and are incoherently superimposed onto the fluorescent signal that is guided through the core of each fiber. However, since the thickness of the faceplate is relatively large (~ 1 cm), the contribution of these unguided fluorescent waves is weaker than the guided fluorescent signal.

Therefore, the faceplate in our on-chip imaging geometry, even though significantly reduces the signal spreading at the detector plane as shown in Fig. 2, also brings its own distortion to the recorded images by creating a unique *incoherent point-spread function* (psf) at the detector plane. The exact spatial form of this 2D incoherent point-spread function is determined by the faceplate periodicity and lattice, numerical aperture of the individual fibers, the distance between the sample plane and the upper surface of the faceplate, as well as the distance between the exit plane of the faceplate and the detector array. Once all these parameters are fixed in our imaging geometry (see Fig. 1 for details), the resulting psf for a given object plane is easily measured using e.g., small diameter fluorescent particles that are imaged at a low concentration. Quite importantly, the physical gap (~ 50 - 100 μm) between the sample and the faceplate planes, together with the gap between the faceplate and the detector planes (~ 75 - 100 μm) ensure that this incoherent point spread function is space invariant all across our imaging FOV, which enables the use of a *single* point spread function for decoding of each object plane as already highlighted in the previous section.

After this brief discussion on the use of the faceplate, let us now expand on the compressive decoding results of our imaging technique. As discussed in the previous section, the main function of the compressive sampling theory in our work is to recover the distribution of the fluorescent points that created the 2D lensless image sampled at the detector array. Knowing the incoherent psf of our system for each object layer, for an arbitrary distribution of fluorescent sources (within e.g., a single micro-channel or a stack of vertical channels), one can easily calculate the expected lensfree image at the detector-array. Using this fact, through a compressive sampling algorithm [26] we optimize the distribution of the fluorescent sources at the object volume based on a given 2D lensless fluorescent measurement. The choice of this compressive decoder [26] is highly suitable for the presented wide FOV fluorescent imaging platform since it is especially designed for sparse signal recovery from large data sets.

To be more specific, our reconstruction/decoding process can be formulized as an l_1 -regularized least squares problem (LSP) [26], such that:

$$\hat{c} = \text{argmin} \left\| I_{\text{det}} - M_{\text{conv}} \cdot \bar{c} \right\|_2 + \beta \cdot \left\| \bar{c} \right\|_1 \quad (4)$$

where $\beta > 0$ is a regularization parameter (typically between 1 and 10); I_{det} is the detected raw fluorescent image at the sensor-array (in a vector form); M_{conv} represents the 2D convolution matrix based on the incoherent point spread function of the system; \bar{c} is the fluorescent source distribution that creates the lensfree image at the detector plane; and

$\left\| \bar{x} \right\|_p = \left(\sum_{i=1}^n |x_i|^p \right)^{1/p}$ represents the l_p norm of vector \bar{x} . For multiple micro-channels that are vertically stacked (see e.g., Figs. 7, 8), there is a separate M_{conv} for each source layer. The compressive decoder used in this work [26] is based on truncated Newton interior-point

method and rapidly provides a sparse solution (\hat{c}) for Eq. (4) especially for large-scale data sets using a non-negativity constraint, which is surely satisfied for fluorescent imaging in general.

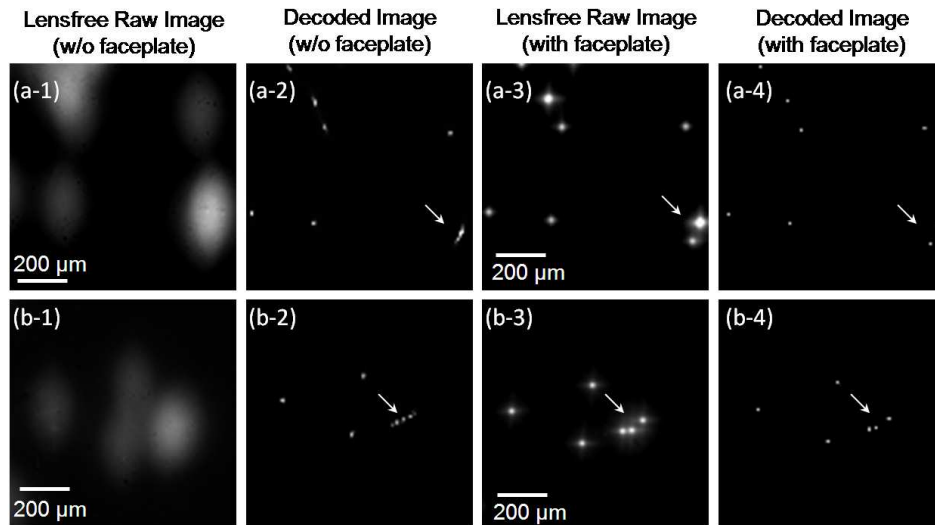


Fig. 3. (a1) shows a digitally zoomed lensfree fluorescent image of 10 μ m particles that is obtained without the use of a faceplate. (a2) illustrates the output of the compressive decoder for the same image in (a1). (a3) shows the same region of interest imaged this time using a faceplate as shown in Fig. 1(a). The compressive decoder output of image (a3) is shown in (a4). The same story is repeated in (b1) through (b4) for a different region of interest. The arrows in these images specifically point to regions where the improvement due to the faceplate becomes apparent to better resolve closely spaced fluorescent particles.

The experimental results that illustrate and quantify the performance of this compressive decoding and reconstruction process are summarized in Figs. 2–8. Specifically, Figs. 2(c3)–2(f3) demonstrate the compressive decoding results of the raw lensfree images acquired with a faceplate. Note that the same compressive sampling algorithm also performs very well even without the use of a faceplate to resolve rather closely spaced fluorescent particles from each other as highlighted in Fig. 3. However, Fig. 3 also compares the performance of the faceplate for decoding of the same field-of-view, which clearly illustrates the superior performance of faceplate based decoded images in terms of resolving closely spaced fluorescent particles without any reconstruction artifacts or ambiguities (e.g., refer to the arrows in Fig. 3).

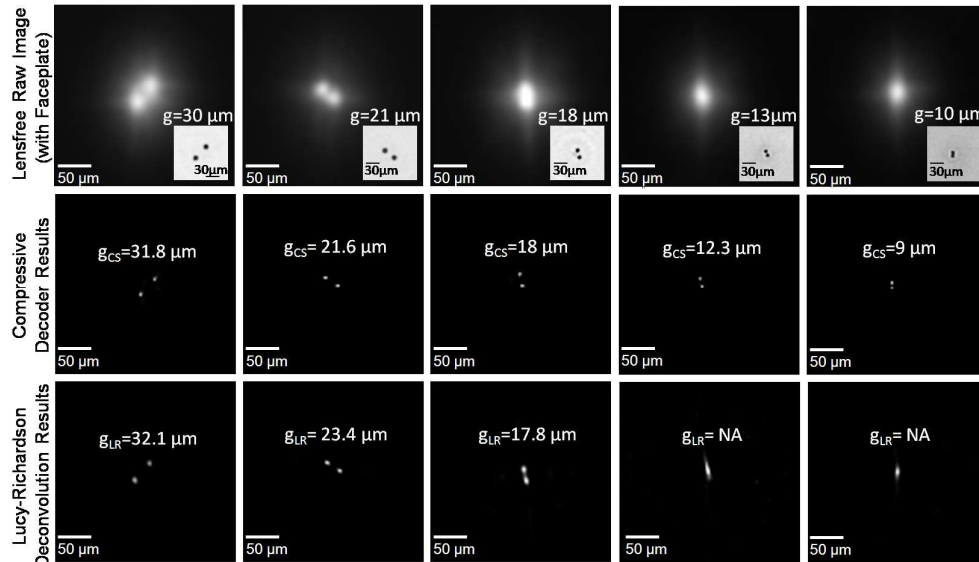


Fig. 4. (Top Row) shows raw lensfree fluorescent images of different pairs of $10\ \mu\text{m}$ diameter particles imaged using the set-up of Fig. 1. As the particles get closer to each other, their signatures in the raw lensfree image become indistinguishable to the bare eye. The inset images in the top row (bottom right corner of each image) illustrate transmission microscope images of the same particles from which the center-to-center distance (g) in each case is calculated only for comparison purposes. (Middle Row) illustrates the results of the compressive decoding process for each lensfree image of the top row. g_{CS} refers to the center-to-center distance of the resolved fluorescent particles in each image, where CS denotes “compressive sampling”. Even for $g = 10\ \mu\text{m}$ case (far right column), we can clearly resolve the fluorescent particles from each other with $g_{\text{CS}} = 9\ \mu\text{m}$. The pixel size in the decoded image is $3\ \mu\text{m}$, whereas the raw lensfree image has been sampled with a pixel size of $W = 9\ \mu\text{m}$ at the detector array, i.e., $N = 9M$. The reason that the reconstructed points for $g_{\text{CS}} = 9\ \mu\text{m}$ case do not touch each other (unlike the microscope image shown in the inset) is that the incoherent point-spread function of the system has been estimated using $10\ \mu\text{m}$ diameter fluorescent particles. Refer to Figs. 5, 6 for imaging of $2\ \mu\text{m}$ diameter fluorescent particles. The computation times of these decoded images vary between 0.1 min to 0.5 min on an Intel Centrino Duo Core, 1GHz PC. (Bottom Row) illustrates the deconvolution results of the Lucy-Richardson algorithm for the same set of lensfree images shown in the top row. g_{LR} refers to the center-to-center distance of the resolved fluorescent particles in each image, where LR denotes “Lucy-Richardson”. The number of iterations [19] in these deconvolution results ranged between 200 and 400, matching with the overall computation time of the CS results for each image. These results indicate that the LR algorithm can resolve particles with $g \sim 18\ \mu\text{m}$, whereas the CS decoder can clearly resolve particles with $g \sim 10\ \mu\text{m}$.

We further quantified the spatial resolution of this compressive decoding process by resolving several closely packed fluorescent micro-particles from each other. Figures 4, 5 and 6 summarize our experimental results which clearly demonstrate resolving two fluorescent particles that are separated by $g \sim 10\ \mu\text{m}$ (center to center). Figure 4 and Fig. 5 are obtained using $10\ \mu\text{m}$ and $2\ \mu\text{m}$ diameter fluorescent particles, respectively; and the pixel size in the decoded images is $3\ \mu\text{m}$ and $2\ \mu\text{m}$, which implies $N = 9M$ and $N \sim 20M$ for Fig. 4 and Fig. 5, respectively. In Fig. 6, we further reduced M by pixel binning at the detector-array such that the pixel size became $W = 18\ \mu\text{m}$. This implies $N = 81M$, which still permitted reconstruction of $2\ \mu\text{m}$ particles that were separated by $g \sim 12\ \mu\text{m}$ (center to center) as shown in Fig. 6. Note that even if the detector array was to directly sample these fluorescent objects in their near-field (hypothetically), the spatial resolution would not be equivalent to $\sim 10\ \mu\text{m}$ due to the large pixel size ($W = 9\ \mu\text{m}$ or $18\ \mu\text{m}$). The computation times of these decoded images are fairly small ranging between 0.1min to 0.5min using an Intel Centrino Duo Core, 1GHz PC.

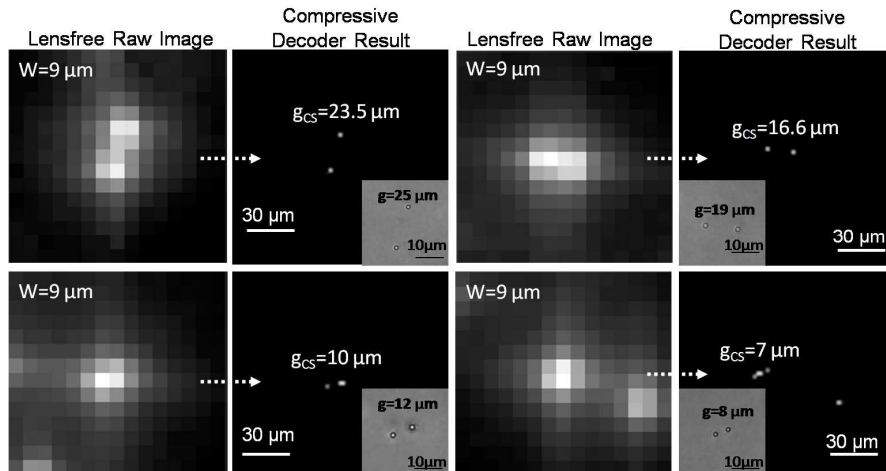


Fig. 5. Same as Fig. 4 except for $2\mu\text{m}$ diameter fluorescent particles. The raw lensfree images are decoded to resolve closely spaced particles from each other. The inset images (bottom right corner of each decoded image) illustrate regular transmission microscope images of the same particles from which the center-to-center distance (g) in each case is calculated for comparison purposes. The bottom row illustrates resolving $2\mu\text{m}$ particles that are separated by $g \sim 12\mu\text{m}$ and $8\mu\text{m}$. The pixel size in the raw lensfree fluorescent images is $W = 9\mu\text{m}$, whereas the pixel size of the decoded images is $2\mu\text{m}$, i.e., $N \sim 20M$. The point-spread function of the system has been estimated using $2\mu\text{m}$ diameter fluorescent particles imaged at a low concentration.

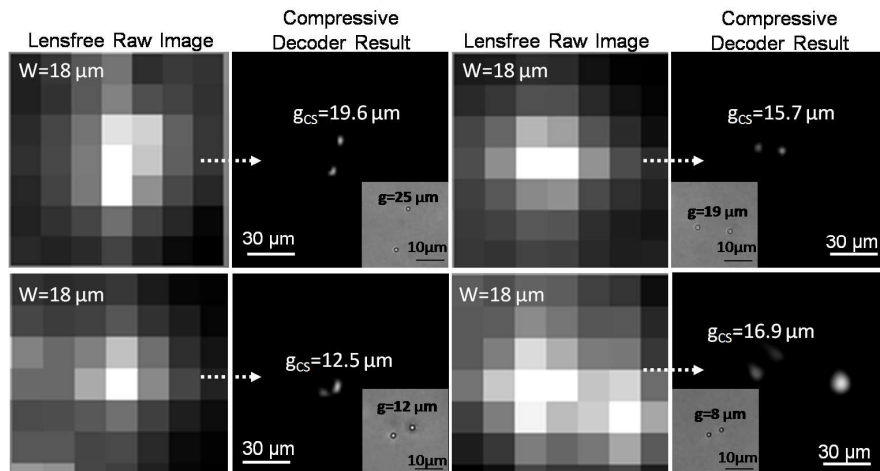


Fig. 6. Same as Fig. 5 ($2\mu\text{m}$ fluorescent particles) except with a pixel size of $W = 18\mu\text{m}$ at the detector-array, such that 4 pixels of the CCD are now binned together. Similar to Fig. 5, the raw lensfree images are decoded to resolve closely spaced fluorescent particles from each other. The pixel size of the decoded images is still $2\mu\text{m}$, same as in Fig. 5, which this time implies $N = 81M$. Because of a significant reduction in M when compared to Fig. 5, the performance of the compressive decoding is relatively degraded, which is especially visible for reconstruction of $g = 8\mu\text{m}$ case (bottom right corner). Regardless, even with $N = 81M$, we have achieved decoding of sub-pixel objects as shown in e.g., $g = 12\mu\text{m}$ case.

Another important dimension of the presented lensfree approach is its ability to reconstruct the distribution of fluorescent micro-objects located at multiple micro-channels that are stacked vertically. This enables to decode the 2D lensfree fluorescent image at the detector-array into a 3D distribution through compressive sampling, which is especially important to further increase the throughput of fluorescent on-chip imaging. A proof of concept demonstration of this capability is presented in Figs. 7 and 8 where the fluorescent

micro-particles ($10\mu\text{m}$ diameter) located at *two* and *three* different micro-channels, respectively, were imaged and decoded all in parallel. In these two experiments the fluorescent channels were vertically separated by 50 and $100\mu\text{m}$, respectively. In Fig. 7 the comparison of the decoding results with and without the faceplate is also provided for the same sample volume, which illustrates the superior performance of the faceplate case for resolving overlapping fluorescent signatures from each other.

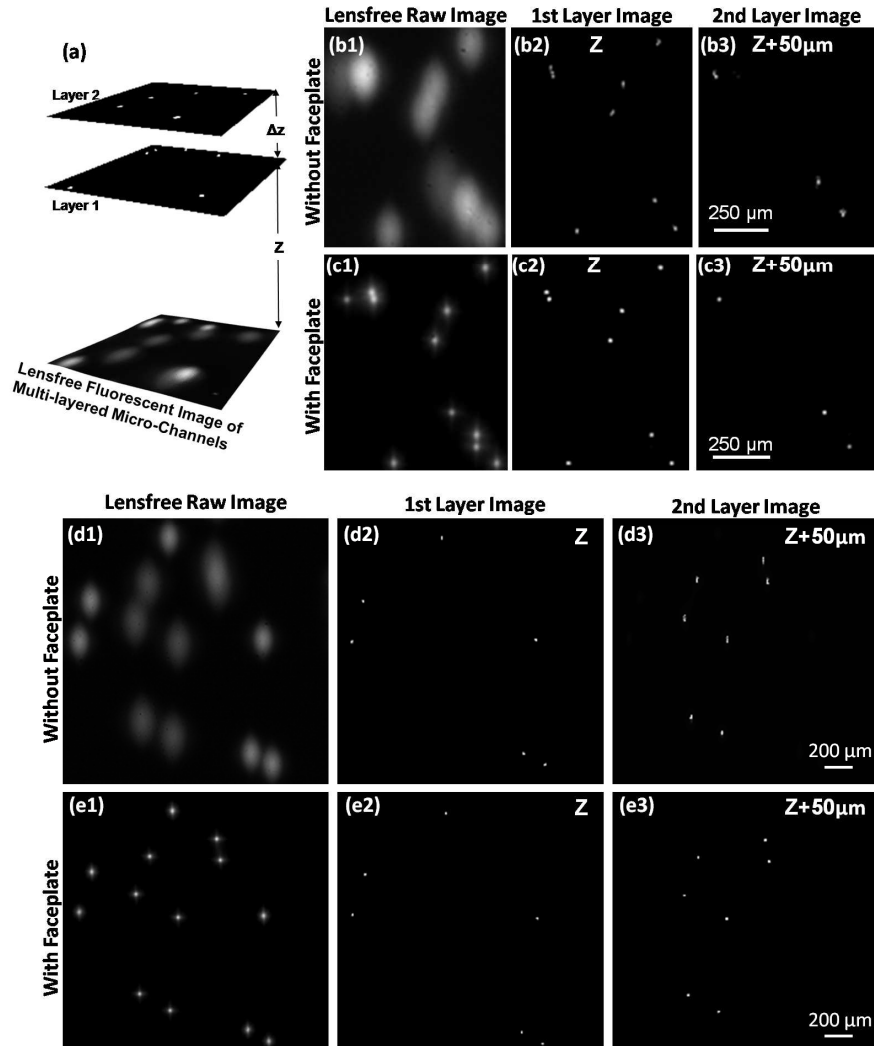


Fig. 7. (a) Lensfree fluorescent imaging of 2 layers that are vertically separated by $\sim 50\mu\text{m}$ is illustrated. (b1) and (d1) show two different digitally cropped regions of the large FOV that are imaged *without* the use of a faceplate (see Fig. 1). The compressive decoding results of these 2 raw lensfree images for each vertical channel are illustrated in (b2-b3) and (d2-d3), respectively. The same regions are also imaged using the faceplate as shown in (c1) and (e1). The compressive decoding results of these 2 raw lensfree images for each vertical channel are also illustrated in (c2-c3) and (e2-e3), respectively.

In general, lensfree on-chip imaging (both transmission [14,15,27,28] and fluorescent [19]) can be thought as an effective compressive sampling encoder. Recent results on “compressive holography” provide an important proof of this for lensfree holographic imaging where a 2D array of pixels at the detector-array was used to reconstruct a 3D volume of voxels without ambiguities [14,15]. Therefore one of the main contributions of these recent

results was to use compressive sampling theory to handle the ill-posed problem of 3D image reconstruction from lensfree in-line holograms. This important contribution remains true regardless of the physical magnification embedded in the lensless imaging system. However, the effectiveness of compressive sampling and the encoding process at the detector array even further increases if there is no physical magnification in the lensless system, such that the detection process now becomes either under- or critically-sampled (as in lensfree holography with unit fringe magnification [27]) or highly ambiguous due to significant spatial overlap and distortion at the detector plane (as in lensfree fluorescent imaging of this work). Therefore, as further discussed in the previous section, the primary function of the compressive decoding process in our work is to remove this spatial ambiguity and distortion due to lensfree and magnification-free operation of our wide-field fluorescent imaging platform.

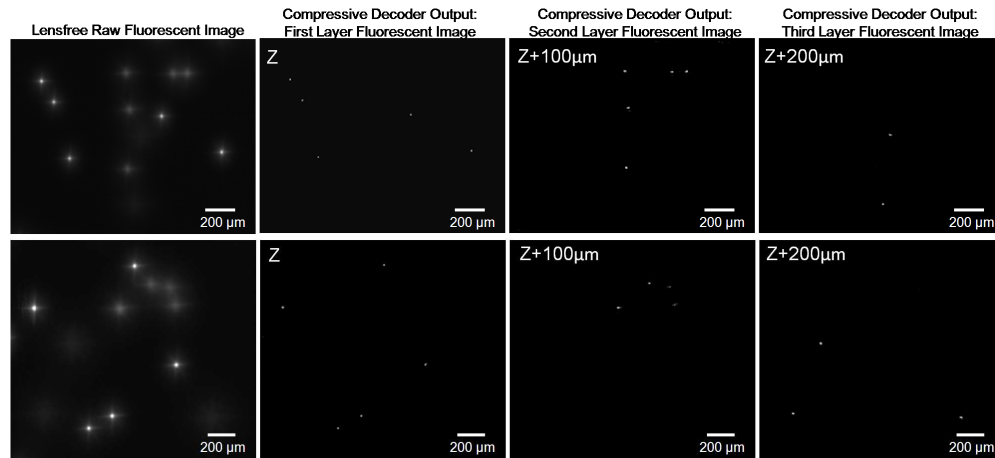


Fig. 8. Same as in Fig. 7, except for 3 fluorescent layers that are vertically separated by ~ 100 μm from each other. Two different regions are imaged using a faceplate, and the raw lensfree images are then decoded to reveal the distribution of the fluorescent particles at each layer. In the raw lensfree images, the fluorescent signatures from the 3rd layer are rather faint and need careful examination to see them with the bare eye, whereas the decoder output for the 3rd layer faithfully resolves their location. Such a computational strength would be quite significant to further increase the throughput in e.g., imaging cytometry experiments.

Finally, we would like to also provide a quantitative comparison of the presented compressive sampling based reconstruction approach over some of the existing deconvolution methods that could potentially be used for the same purpose. One such numerical recipe is the Lucy-Richardson algorithm [29–31] which relies on the knowledge of the incoherent point spread function to iteratively converge to the maximum-likelihood estimation of the fluorescence source distribution based on the detected image. This algorithm is not restricted to sparse objects only and has been shown to be quite effective converging within typically a few hundred iterations to the source distribution [19]. A comparison of the performance of this algorithm against compressive sampling based reconstruction is demonstrated in Fig. 4 (bottom row), which clearly indicates the advantages of the compressive decoding approach especially in terms of spatial resolution. Figure 4 demonstrates that, for the same set of lensless fluorescent measurements, the compressive decoder achieves $\sim 10\mu\text{m}$ resolution, while the Lucy-Richardson deconvolution algorithm achieves $\sim 20\mu\text{m}$. This behavior is intuitively expected since the Lucy-Richardson algorithm does not use the sparsity of the object as an optimization constraint. Besides resolution, another important difference between the two approaches is that unlike compressive sampling which can easily perform multi-layer reconstruction for sparse objects as illustrated in Figs. 7–8, the Lucy Richardson algorithm would need to be significantly modified to handle 3D reconstruction. On the other hand, conventional deconvolution algorithms that do not rely on a sparsity constraint (such as the

Lucy Richardson algorithm) could potentially better handle highly dense fluorescent samples, where the sparsity condition of the object is no longer satisfied.

Before we conclude, we would like to also point out that the compressive decoding results of this work (in particular Figs. 4–8) could also be extended to conventional *lens-based* fluorescent microscopy, and in particular to recent fluorescent super-resolution approaches including PALM and STORM [24,25]. A significant benefit of the use of a compressive decoder in such super-resolution approaches would be to reduce the number of frames that is required for 2D and 3D fluorescent imaging. It is a known fact that these super-resolution techniques work based on localization accuracy and they have to reject a frame if two fluorophores within a point-spread function width emit at the same time. Some of these normally rejected fluorescent frames could potentially be decoded using compressive sampling approaches to significantly reduce the imaging time of fluorescent imaging in these super-resolution approaches. Potentially, such a compressive decoding approach, together with the computational power of next-generation graphics processing units (GPUs), may in the near-future lead to “real-time” super-resolution fluorescent microscopy.

4. Conclusions

While conventional fluorescent microscopy is already quite powerful, there is still a significant need for high-throughput and compact fluorescent imagers that can potentially be used with large format micro-fluidic devices to perform rapid imaging/screening of e.g., rare cell events or DNA/protein micro-arrays. Towards this end, here we have introduced an on-chip fluorescent imaging modality that achieves a spatial resolution of $\sim 10\mu\text{m}$ without the use of any lenses over an ultra-large field of view of $>8\text{ cm}^2$ based on the compressive sampling theory. In this lensfree fluorescent imaging technique, the samples of interest are positioned onto a chip and are pumped through a prism interface, where the excitation beam is filtered out by total internal reflection occurring at the bottom facet of the sample holder. The fluorescent emission from the sample volume is then collected using a fiber-optic faceplate which delivers the fluorescent signal onto the detector plane through a unique incoherent point spread function. The detected 2D lensless fluorescent image is rapidly processed using a compressive sampling algorithm to reconstruct the sparse fluorescent source distribution at the sample volume covering $>8\text{ cm}^2$ FOV. Such a wide-field and compact fluorescent imaging platform could especially be very important for high-throughput cytometry, rare cell analysis as well as for micro-array research.

Acknowledgments

The authors acknowledge the support of the Okawa Foundation, Vodafone Americas Foundation, DARPA DSO (under 56556-MS-DRP), NSF BISH program (under Awards # 0754880 and 0930501), NIH (under 1R21EB009222-01 and the NIH Director’s New Innovator Award - Award Number DP2OD006427 from the Office of The Director, National Institutes of Health), AFOSR (under Project # 08NE255). A. Ozcan also gratefully acknowledges the support of the Office of Naval Research (ONR) under the Young Investigator Award 2009.